

A Bimodal MRI-Traceable Nanozyme with Immune-Activated Capability for Immunotherapy of Lung Metastases

Qiuyi Xu,^{||} Sha Li,^{||} Maosong Qiu, Xiaoxun Liu, Meiju Sui, Lei Zhang, Xin Zhou, and Shizhen Chen*Cite This: *ACS Appl. Bio Mater.* 2025, 8, 5818–5829

Read Online

ACCESS |



Metrics & More



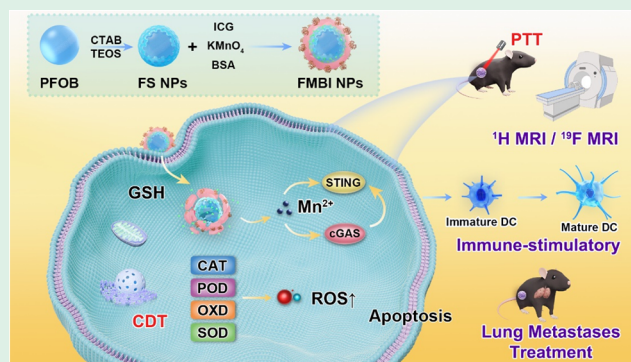
Article Recommendations



Supporting Information

ABSTRACT: The therapeutic efficacy of cancer is greatly hampered by hypoxia, overexpressed glutathione (GSH) in the tumor microenvironment (TME), and the high propensity for tumor metastasis. Developing advanced diagnostic and therapeutic strategies capable of destroying tumors holds great promise. Herein, multifunctional manganese-based nanoparticles (FMBI NPs) with multiple nanozyme activities and GSH-depleting capabilities were designed to enhance cancer therapy by remodeling the TME. The release of Mn ions from FMBI NPs under TME conditions can modulate the tumor stroma, activate the cyclic GMP–AMP synthase-stimulator of interferon genes (cGAS-STING) pathway, and promote immunogenic cell death (ICD) in tumor cells, which has been demonstrated through various cellular studies. Notably, systemic immune activation mediated by FMBI NPs effectively inhibits lung metastasis while simultaneously enabling ¹H and ¹⁹F MRI for tumor visualization. This approach opens the way to image the biodistribution of the nanoagent *in vivo* and to monitor its therapeutic efficacy toward tumors noninvasively with MRI.

KEYWORDS: ¹⁹F MRI, cGAS-STING, nanozymes, immunogenic death, immunotherapy



1. INTRODUCTION

Cancer remains a grave public health challenge, underscoring the imperative for effective therapeutic strategies.^{1–3} Recent advancements have brought diverse treatment strategies,^{4,5} including chemodynamic therapy (CDT), sonodynamic therapy (SDT), photothermal therapy (PTT), and photodynamic therapy (PDT). However, surgical resection, chemotherapy, and radiotherapy remain the mainstay in clinical settings.^{6,7} Given the complex and heterogeneous nature of tumors as well as the limitations of existing therapeutic approaches, the eradication of tumor cells via conventional single-modality treatments proves to be a formidable challenge. To address this challenge, multimodal synergistic therapy has been developed, integrating the benefits of multiple therapies to enhance treatment efficacy.^{8,9} Despite these advancements, existing therapeutic approaches remain ineffective in eliminating cancer cells during the initial phases of tumor metastasis. Tumor immunotherapy stands out as it possesses the potential to activate the immune system and eradicate metastatic tumor cells¹⁰ and is thus recognized as the optimal strategy for treating tumor metastasis.

Various cancer treatment methods can induce immunogenic cell death (ICD),¹¹ which is crucial for effective tumor immunotherapy. Nanotechnology enhances ICD by improving targeted drug delivery, amplifying drug accumulation in tumors, enabling the synchronous application of multiple

therapies, and enabling precise dosage control.¹² These advancements refine the tumor microenvironment and bolster the immune response, ultimately improving treatment outcomes.^{13,14} The emerging field of metal immunology has garnered attention as studies increasingly demonstrate that several transition metals can provoke autoimmunity.¹⁵ Notably, manganese (Mn)-based nanoparticles, particularly those with simple compositions like manganese oxide (MnO_x), exhibit multifaceted roles in augmenting tumor magnetic resonance imaging (MRI), modulating the tumor microenvironment (TME), facilitating CDT, and boosting immunotherapy.^{16,17} Recent studies have underscored manganese's role as an immunostimulant. The cyclic GMP–AMP synthase-stimulator of interferon genes (cGAS-STING) pathway can be activated by Mn²⁺ ions directly and the cyclic guanosine monophosphate-adenosine monophosphate (cGAMP)-mediated stimulation of STING will be potentiated.^{18–20} It leads to an elevated production of type I interferons (IFNs), thereby optimizing antigen presentation, promoting dendritic cell

Received: March 24, 2025

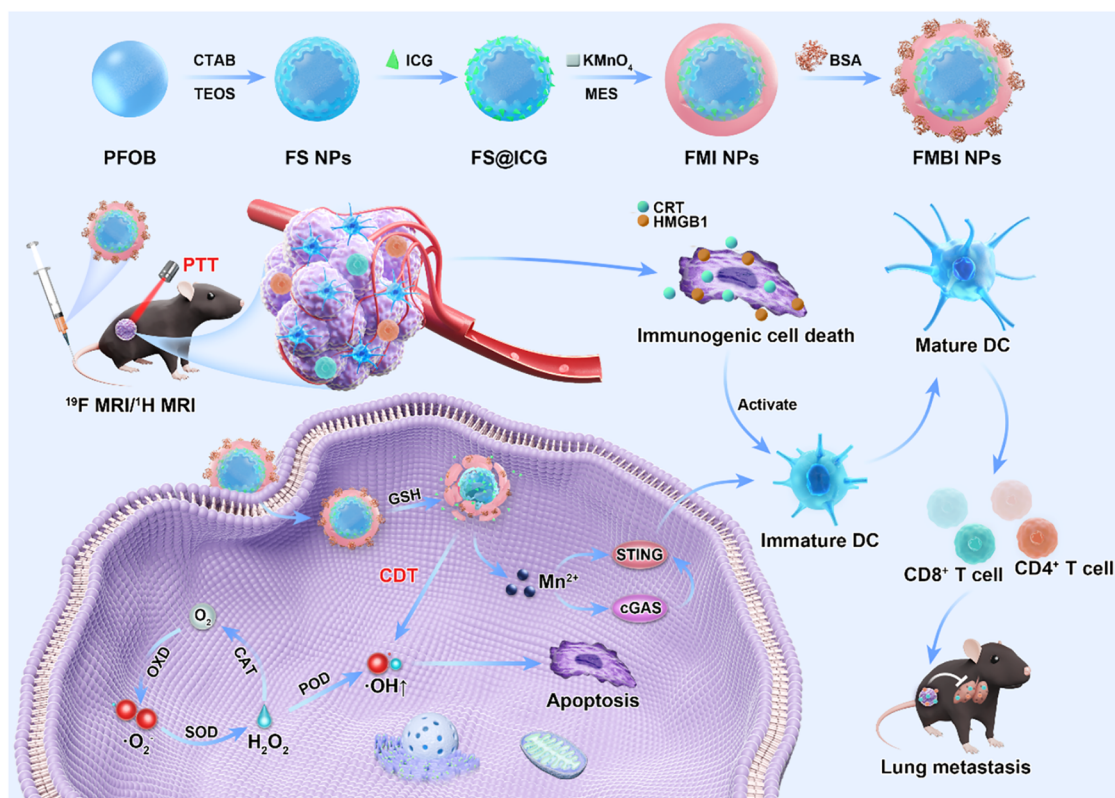
Revised: June 8, 2025

Accepted: June 10, 2025

Published: June 16, 2025



Scheme 1. Schematic Illustration of the Preparation of FMBI NPs and the $^1\text{H}/^{19}\text{F}$ MRI-Guided Synergistic PTT/CDT Therapeutic Strategy^a



^aThis TME-responsive, manganese-boosted catalytic therapy is in conjunction with the activation of the cGAS-STING pathway.

(DC) maturation, and enhancing antitumor T cell responses.²¹ Leveraging the advantages of manganese-based nanoparticles, researchers have developed innovative nanoplatforms to enable effective combination immunotherapies targeting the cGAS-STING pathway. These include amorphous porous manganese phosphate nanoparticles,²² biomaterialized manganese dioxide (MnO_2),²³ Mn^{2+} -liganded micelles,²⁴ and metal polyphenolic networks.^{25,26}

Manganese-based nanoparticles hold promise for tumor therapy due to their diverse functionalities.^{27,28} These nanoparticles have also been designed to exhibit enzyme-like activities (nanozymes), positioning them as promising candidates for therapeutic nanodrugs.^{29,30} Manganese-based nanozymes can elevate intracellular reactive oxygen species (ROS) levels via Mn^{2+} -mediated Fenton-like reactions or by reducing GSH through Mn^{4+} -mediated redox reactions.^{31,32} Nevertheless, integrating manganese's beneficial properties into a single nanoplatform to enhance cancer treatment efficacy is still an underexplored domain, particularly in the convergence of MRI, metal-based nanozymes, and immunostimulants. Thus, there exists a compelling exigency to engineer multifunctional manganese-based nanoparticles with simple compositions to achieve these composite functionalities and improve tumor immunotherapy efficacy.

In this study, we developed fluorine-containing manganese-based core-shell nanoparticles with ICG-loading and BSA-coating (FMBI NPs) that can deplete GSH and activate the immune response against tumors while enabling multinuclear $^1\text{H}/^{19}\text{F}$ MRI in a melanoma model (Scheme 1). FMBI NPs exhibit dual enzymatic activities similar to oxidase (OXD) and

peroxidase (POD), generating abundant ROS to facilitate tumor cell elimination. Additionally, FMBI NPs relieve tumor hypoxia by mimicking catalase (CAT) activity, thus transforming the TME. The depletion of GSH in the TME promotes the release of Mn^{2+} from FMBI NPs, further enhancing the immune responses within the tumor. The local application of FMBI NPs promotes the release of ICD signals, which leads to damage-associated molecular patterns (DAMPs) in tumor cells and activation of systemic immunity. Concurrently, Mn^{2+} discharged from the nanoparticles synergizes with cGAMP to strongly activate the cGAS-STING pathway in DCs within nearby lymphoid tissues, initiating a cascade of immune responses. This comprehensive approach enhances systemic immune functions and hampers lung tumor metastasis. Additionally, Mn^{2+} accumulation in tumors also facilitates efficient ^1H T_1 -weighted MRI. Following the GSH response, the paramagnetic relaxation enhancement (PRE) effect of MnO_x decreases, leading to an enhanced ^{19}F MRI signal within the nanoparticles. Simultaneously, the release of free Mn^{2+} from FMBI NPs further enhances the ^1H T_1 -weighted MRI signal. In essence, our study introduces a multifaceted nanoplatform that integrates multiple therapeutic and imaging modalities, encompassing enzymatic activity, photothermal therapy, immunotherapy, and MRI.

2. RESULTS AND DISCUSSION

2.1. Synthesis and Characterizations of FMBI NPs.

The synthesis of FMBI NPs and fluorine-accumulated silica nanoparticles (FS NPs) is outlined in Scheme 1 and elaborated in the Supporting Information.^{33,34} The FMBI NPs showed a

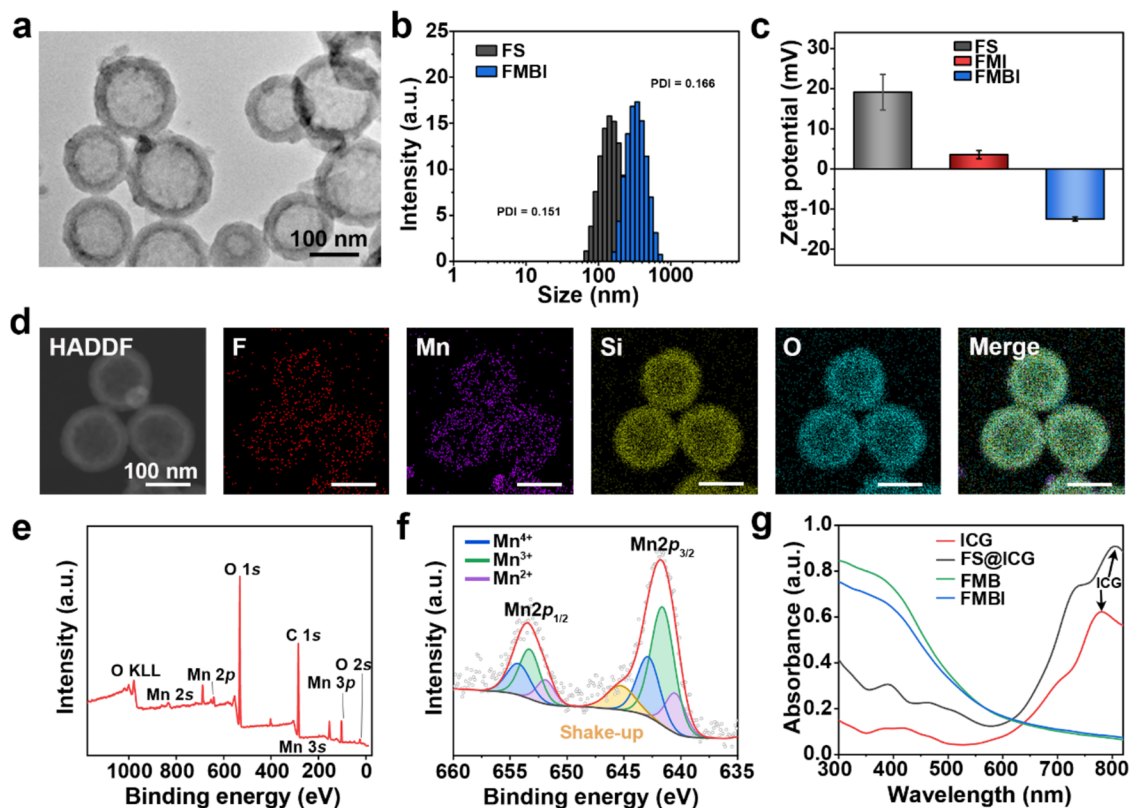


Figure 1. Characterizations of FMBI NPs. (a) Representative TEM image of FMBI NPs. (b) Size distributions of FS NPs and FMBI NPs as measured by DLS. (c) ζ -Potential of FS, FMI, and FMBI NPs. (d) Corresponding elemental mapping of FMBI NPs. (e) Survey XPS spectrum and (f) Mn 2p XPS spectrum of FMBI NPs. (g) UV–vis–NIR absorption spectra of ICG, FS@ICG, FMB, and FMBI NPs.

rough surface morphology and spherical core–shell structures with an average size of about 145 nm, according to the representative transmission electron microscopy (TEM) image (Figure 1a). Dynamic light scattering (DLS) affirmed that the average hydrated particle size of FMBI NPs (302.6 nm, PDI = 0.166) is larger than that of FS NPs (101.8 nm, PDI = 0.151). The ζ -potential decreased from 19.1 ± 4.4 mV for FS NPs to -12.5 ± 0.5 mV for FMBI NPs (Figure 1b,c), which can be ascribed to the coating of MnO_x and the presence of negatively charged BSA. The distribution of manganese (purple) and fluorine (red) within FMBI NPs was identified using high-angle annular dark-field (HAADF) imaging in conjunction with energy-dispersive X-ray (EDX) element mapping (Figure 1d). The Mn 2p high-resolution spectrum obtained from X-ray photoelectron spectroscopy (XPS) analysis comprising bivalent states Mn 2p_{1/2} and Mn 2p_{3/2} confirmed the dominance of Mn³⁺ (48.47%) and Mn⁴⁺ (26.98%), respectively, while Mn²⁺ was present at a lower proportion of 15.81% (Figure 1e,f). Moreover, changes in the UV–vis–NIR absorption spectra suggested the successful loading of indocyanine green (ICG) onto the FS@ICG NPs, and the absorption peak of ICG was further burst after encapsulation of the MnO_x shell in FMBI NPs (Figure 1g).

2.2. The Catalytic Activity of FMBI NPs. It is well-established that low-valence manganese (Mn²⁺ and Mn³⁺) exhibits POD- and OXD-like activities, while high-valence manganese (Mn⁴⁺) facilitates the depletion of GSH.³⁵ Consequently, the hybrid valence states of Mn ions confer FMBI NPs with multifunctional enzyme-like activities and GSH-depletion capability. Previous studies have shown that most MnO_x nanomaterials exhibit broad pH-dependent CAT-

like activity with optimal performance across a wide pH range,³⁶ which enable the catalytic decomposition of H_2O_2 into H_2O and O_2 . The CAT-like activity of FMBI NPs was confirmed by measuring O_2 generation with a dissolved oxygen meter. Enzyme activity assays were conducted at a physiological temperature of 37 °C and a slightly acidic pH of 6.4 to simulate the tumor environment. The results revealed that the CAT-like activity of FMBI NPs correlated with the enzyme concentration, leading to varied levels of O_2 production (Figure 2a). Subsequently, an expanded investigation was conducted on the POD- and OXD-like activities of FMBI NPs. These nanozymes are known to catalyze the decomposition of H_2O_2 into $\cdot\text{OH}$ and $\cdot\text{O}_2^-$ by transferring electrons to O_2 . These catalytic processes led to the oxidation of 3,3',5,5'-tetramethylbenzidine (TMB) into its blue oxidized form (oxTMB), which showed a characteristic UV absorbance at 370 and 652 nm. The POD-like activity of FMBI NPs (pH = 6.4) exhibited a correlation between the UV–vis absorbance of oxTMB and nanozyme concentration (Figure 2b). The generation of $\cdot\text{OH}$ was further confirmed using the electron spin resonance (ESR) technique with 5,5-dimethyl-1-pyrroline-*N*-oxide (DMPO) as the spin-trapping agent. FMBI NPs produced a Fenton-like reaction quartet signal pattern (1:2:2:1), similar to the $\text{FeCl}_2\text{--H}_2\text{O}_2$ control, but with higher intensity (Figure 2c). Likewise, the activity of the OXD-like enzyme of FMBI NPs was evaluated via the TMB colorimetric assay. The UV absorbance of the corresponding oxTMB was found to be dependent on the OXD enzyme concentration, following the direct addition of the color developer and FMBI NPs under acidic conditions (Figure 2d). The POD-like activity showed a lower absorbance than the OXD-like activity

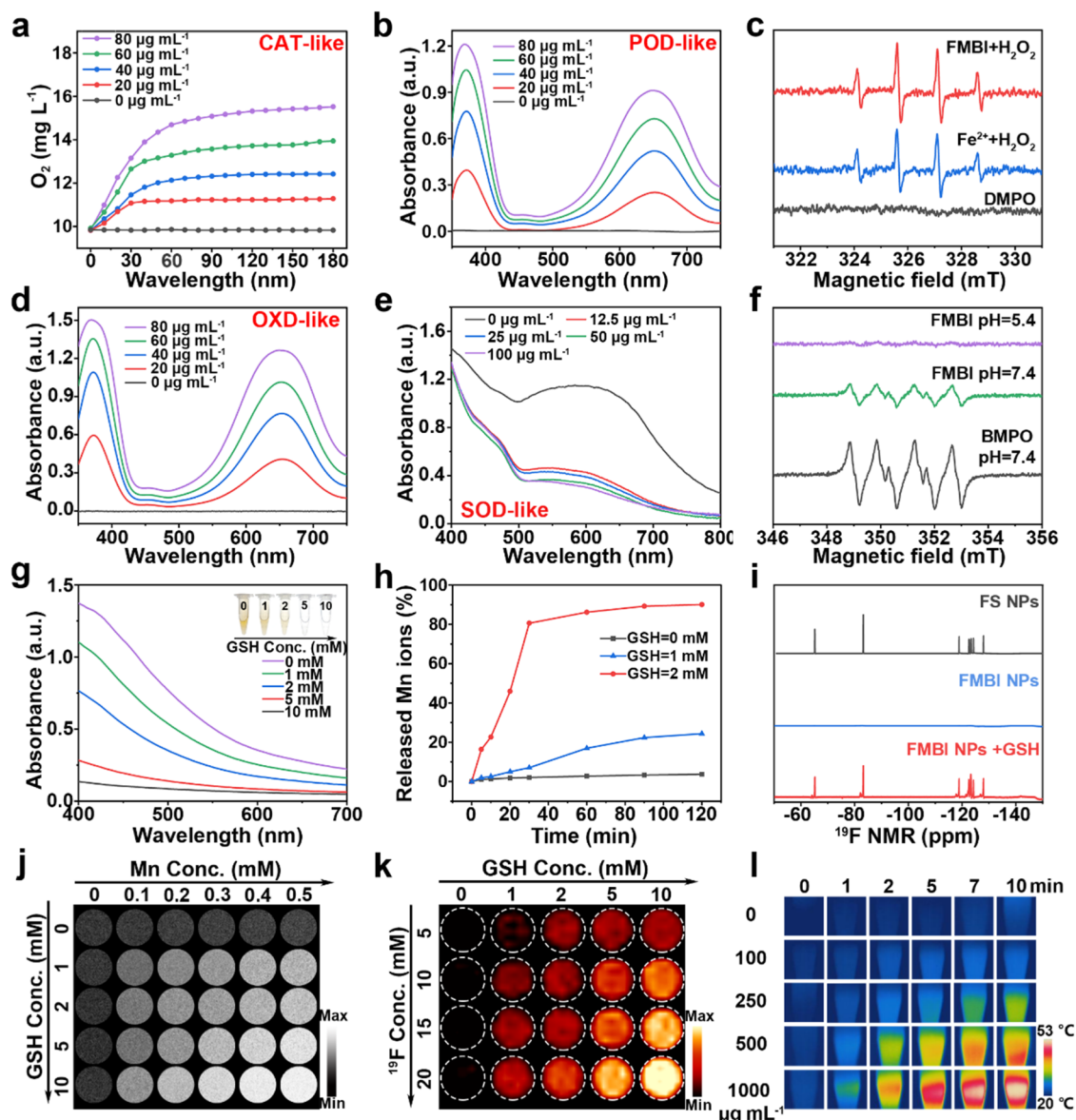


Figure 2. Multienzyme-like activities, GSH depletion, NIR, and MRI performance of FMBI NPs. (a) CAT-like and (b) POD-like activities of FMBI NPs. (c) ESR spectra of FMBI NP-mediated generation of $\bullet\text{OH}$. (d) The OXD-like and (e) SOD-like activities of FMBI NPs. (f) ESR spectra for $\bullet\text{O}_2^-$ of FMBI NPs. (g) Concentration-dependent GSH consumption by FMBI NPs. (h) Cumulative Mn ion release profiles at various GSH concentrations. (i) ^{19}F NMR spectra of FS NPs and FMBI NPs with or without GSH treatment. (j) ^1H T_1 -weighted MRI and (k) ^{19}F MRI images of FMBI NPs at different GSH concentrations. (l) NIR thermal images of FMBI NP aqueous solutions at various concentrations under an 808 nm laser irradiation (0.5 W cm^{-2} , 10 min).

upon H_2O_2 addition, demonstrating the existence of a cascade reaction pathway with FMBI NPs. Nitro blue tetrazolium (NBT) assay was conducted to detect superoxide dismutase (SOD)-like activity. It was observed that the UV absorbance and solution color gradually declined with higher concentrations of FMBI NPs, indicating effective SOD-like activity (Figure 2e). The SOD enzyme activity was further confirmed by employing 5-tert-butoxycarbonyl-5-methyl-1-pyrroline-*N*-oxide (BMPO) to capture $\bullet\text{O}_2^-$ generated by the xanthine/xanthine oxidase system (Figure S1, Supporting Information). Upon the addition of FMBI NPs, the ESR signal intensity of $\bullet\text{O}_2^-$ (a characteristic signal of 1:1:1:1) was notably reduced under acidic conditions compared to that under physiological conditions ($\text{pH} = 7.4$), suggesting that FMBI NPs possess SOD-like activity (Figure 2f).

The GSH-depletion ability of FMBI NPs was also evaluated due to the presence of the high valence state of Mn ions. Upon adding 5,5-dithiobis (2-nitrobenzoic acid) (DTNB), a GSH indicator, to the mixture of FMBI NPs and GSH, the characteristic UV absorption at 412 nm decreased with increasing GSH concentration (Figures 2g and S2). The reaction of GSH with FMBI NPs leads to an increased level of oxidative damage and promotes an antitumor immune response through the generation of Mn^{2+} . Compared to normal physicochemical conditions, the TME exhibits more extreme physicochemical characteristics, permitting reactions with MnO_x nanomaterials to release Mn ions.³⁷ The TME-responsive Mn ion release from FMBI NPs was examined in a TME-mimic *in vitro* system via ICP-OES. FMBI NPs were initially incubated at $37\text{ }^\circ\text{C}$ in PBS ($\text{pH} = 6.4$) with different

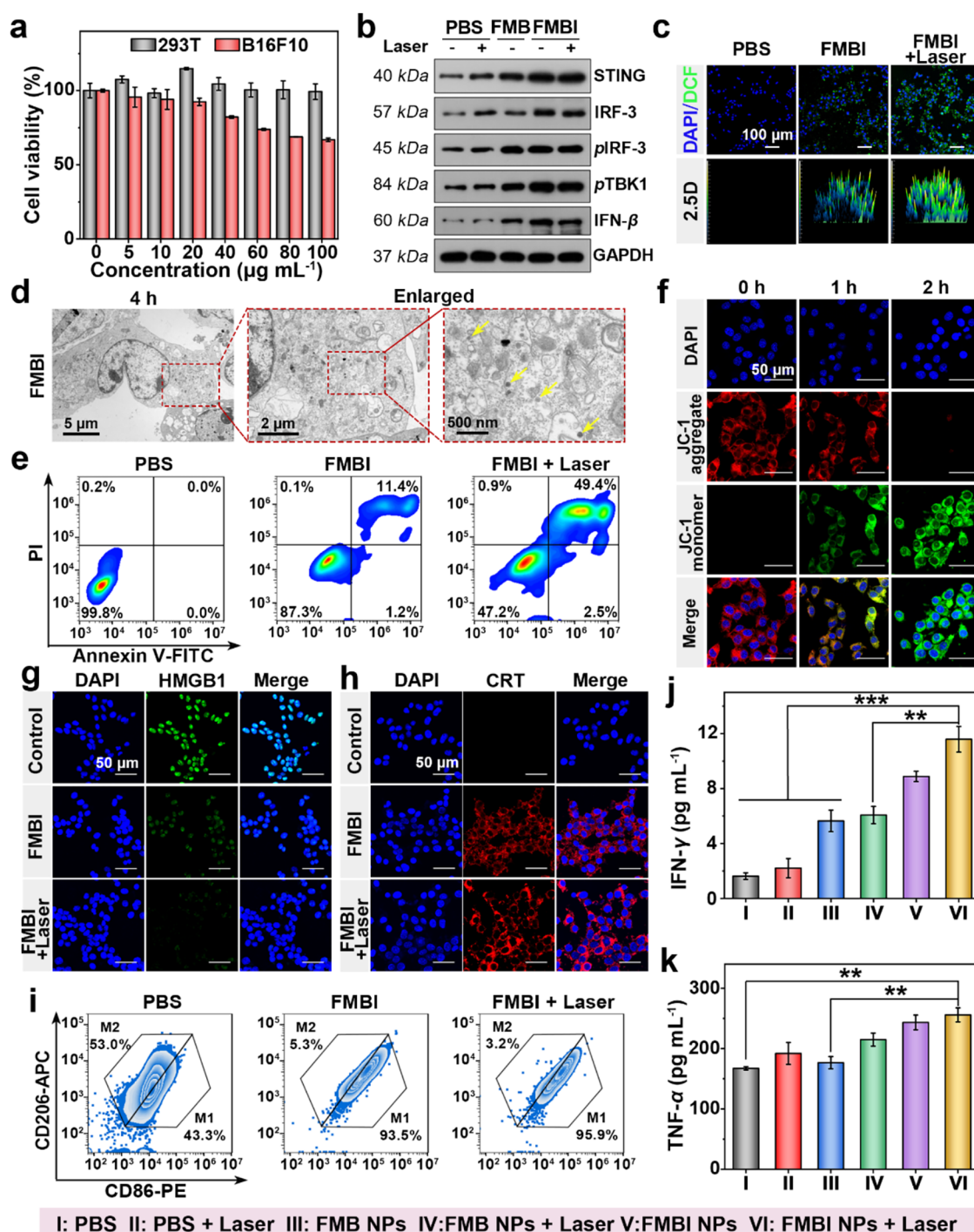


Figure 3. Intracellular behavior and immune activation effect of FMBI NPs. (a) Cell viability of the 293T or B16F10 cells after incubation with different concentrations of FMBI NPs for 24 h (mean \pm SD, $n = 3$). (b) Western blot analysis of STING, IRF-3, p-IRF-3, p-TBK1, and IFN- β protein expressions in B16F10 cells after treatment with PBS, FMB NPs, and FMBI NPs with or without laser irradiation. (c) CLSM images showing intracellular total ROS production. (d) Bio-TEM images of B16F10 cells incubated with FMBI NPs for 4 h. (e) Flow cytometry scatter diagram showing B16F10 cell apoptosis after different treatments (stained with Annexin V-FITC/PI apoptosis kit). (f) CLSM images of the mitochondrial membrane potential ($\Delta\Psi_m$) performance. CLSM images of intracellular (g) CRT and (h) HMGB1 expression after incubation with PBS (control), FMBI NPs, and FMBI NPs plus laser for 4 h. (i) Representative images of RAW264.7 analyzed by flow cytometry after treatment with different conditions for 24 h. Quantitative analysis of the cytokines (j) IFN- γ and (k) TNF- α secreted by B16F10 cells in the medium after different treatments. n.s. not significant, ** $p < 0.01$, and *** $p < 0.001$.

concentrations of GSH. The results showed that the release rates of Mn ion from FMBI correlated with GSH concentrations (Figures 2h and S3). Specifically, at a GSH concentration of 2 mM, 90.08% of the Mn ions were released within 2 h. In contrast, in the absence of GSH (pH = 5.4), only

7.76% of Mn ions were released over the same period. These findings suggested that FMBI NPs can selectively release Mn ions under the TME conditions.

Considering the release of the Mn ion, the GSH-mediated enhancement of ^1H T_1 -weighted MRI contrast and longi-

tudinal relaxivity (r_1) of FMBI NPs were investigated. First, the longitudinal relaxation time of FMBI NPs with or without GSH at various pH values (pH = 7.4, 6.4, and 5.5) was measured. Notably, r_1 increased significantly with higher GSH concentrations. Specifically, the r_1 value of FMBI NPs increased from 0.23 $\text{mM}^{-1} \text{s}^{-1}$ to 6.09, 5.41, 6.10, and 4.38 $\text{mM}^{-1} \text{s}^{-1}$ at GSH concentrations of 1, 2, 5, and 10 mM (pH = 6.4), respectively (Figure S4). Subsequently, ^1H T_1 -weighted MRI phantom images of FMBI NPs were acquired by using a 9.4 T MRI system. These images showed an increase in signal intensity corresponding to higher GSH concentrations (Figure 2j). Similarly, r_1 was tested at different pH values but did not show significant enhancement due to the GSH-dependent mechanism of Mn ion release (Figures S5 and S6). The MnO_x layer surrounding the nanoparticle attenuates the ^{19}F NMR signal of PFOB through the PRE effect. However, in a TME-responsive manner, the disintegration of the MnO_x layer restores the ^{19}F NMR signal. To examine changes in ^{19}F intensity, FMBI NPs were incubated with a 10 mM GSH solution (pH = 6.4). A marked resurgence of the ^{19}F NMR signal (-83.19 ppm) was observed, signifying the ^{19}F NMR signal turn-on behavior of the probe (Figure 2i). With increasing GSH concentrations, the ^{19}F MRI signal intensity of FMBI NPs increased rapidly, indicating the GSH-mediated activation of ^{19}F MRI (Figure 2k).

The incorporation of ICG endows FMBI NPs with photosensitizing properties. To investigate the photothermal performance of FMBI NPs, various concentrations of FMBI NPs were subjected to NIR irradiation using an 808 nm laser (0.5 W cm^{-2} , 10 min), and infrared thermal images were captured (Figure 2l). The final temperature of the FMBI NP solution was found to be concentration-dependent under identical irradiation conditions (Figure S7). Additionally, FMBI NPs maintained a stable photothermal performance over four cycles of laser on/off, achieving a photothermal conversion efficiency of 37.5% (Figures S8–S10). The above results demonstrate that FMBI NPs possess favorable photothermal properties.

2.3. Cellular Endocytosis and ROS Generation of FMBI NPs. Given the ability of FMBI NPs to generate ROS and deplete GSH, the potential for manganese-catalyzed immune activation mediated by FMBI NPs at the cellular level was investigated. The cytotoxicity of FMBI NPs in human embryonic kidney cells (293T) and mouse skin melanoma cells (B16F10) was first assessed by using the standard Cell Counting Kit-8 (CCK-8) assay (Figure 3a). After 24 h of cocubation, FMBI NPs demonstrated significant cytotoxicity in B16F10 cells starting at a concentration of $60 \mu\text{g mL}^{-1}$. With FMBI NP concentration increased to $100 \mu\text{g mL}^{-1}$, the cell viability decreased to $65.8 \pm 4.4\%$. In contrast, negligible cytotoxicity was observed in 293T cells, even at a concentration of $100 \mu\text{g mL}^{-1}$. The cellular uptake behavior of the nanoparticles was performed using confocal laser scanning microscopy (CLSM). The internalization of rhodamine B-labeled FMB NPs by B16F10 cells demonstrated a gradual augmentation, culminating in peak levels following 4 h of cocubation (Figure S11). Next, the phagocytic behavior of FMBI NPs was examined by using biological transmission electron microscopy (Bio-TEM). The aggregated nanoparticles were taken up by tumor cells and wrapped into the endosomal system after 4 h of cocubation (Figures 3d and S12). These results implied that FMBI NPs were effectively internalized by B16F10 cells, a critical step for their cytotoxic efficacy against

tumor cells. The low level of adhesion between melanoma cells makes it difficult to form compact cell aggregates. Therefore, A549 cells were used as multicellular spheroid model to evaluate the permeability of FMBI NPs in TME. Following treatment with rhodamine B (RB)-labeled FMBI NPs under designated conditions, multicellular spheroids were imaged using a CLSM. Notably, an increased infiltration of FMBI NPs, which was observed after treatment with 1 mM GSH, as evidenced by the strong red fluorescence distributed throughout the whole multicellular spheroids (Figure S13). Upon GSH exposure, the ζ -potential shifted from -37.3 to -4.2 mV, indicating a substantial reduction in surface electronegativity (Figure S14).

To investigate the intracellular toxicity of FMBI NPs toward B16F10 cells, the cellular ROS levels were detected using a ROS probe, 2,7-dichlorofluorescein diacetate (DCFH-DA), which reacts with ROS to produce 2,7-dichlorofluorescein (DCF) with green fluorescence. B16F10 cells cocubated with FMBI NPs displayed increased green fluorescence intensity compared to the control group, and the fluorescence brightened upon an 808 nm laser irradiation, corroborating the flow cytometry results (Figures 3c and S15). These findings suggested that ROS generation occurred in a laser-activated manner. Previous studies have shown that elevated intracellular ROS can induce apoptosis through mitochondrial impairment and DNA double-strand breaks. The JC-1 fluorescent probe was used to measure the mitochondrial membrane potential ($\Delta\Psi_m$) in order to investigate mitochondrial damage. The presence of red fluorescence from the JC-1 aggregates indicates an intact mitochondrial membrane potential, whereas the formation of JC-1 monomers, which emit green fluorescence, reveals depolarized mitochondria with compromised membranes. Following cocubation with FMBI NPs, B16F10 cells exhibited a significant decrease in red fluorescence and an increase in green fluorescence over time, suggesting a reduction in cellular $\Delta\Psi_m$ (Figure 3f). Apoptosis assays were conducted to ascertain cell death by using the Annexin V-FITC/PI staining method. After treating B16F10 cells with FMBI NPs for 4 h with subsequent laser irradiation, 49.4% of cells were in the late apoptotic and early necrotic stages, as observed via flow cytometry (Figure 3e). Confocal microscopy live–dead staining of B16F10 cells further confirmed that FMBI NPs plus laser treatment induced apoptosis (Figure S16). These results suggest that FMBI NPs exhibit potential for synergistic therapy, demonstrating effective antitumor activity.

2.4. The Enhanced Antitumor Immune Response Induced by FMBI NPs. ROS and oxidative stress play essential roles in evoking ICD. Considering the ability of FMBI NPs to efficiently generate ROS and consume GSH, we subsequently explored their potential to initiate ICD. The release of DAMPs from dying tumor cells represents a critical hallmark of ICD. Notably, the presence of key DAMPs, including calreticulin (CRT) and high-mobility group box-1 (HMGB1)—prototypical proteins in this process—was assessed following exposure to FMBI NPs. Immunofluorescence assays revealed a marked increase in intracellular CRT fluorescence 4 h post-treatment, signifying elevated CRT expression (Figure 3g). In addition, diminished intracellular HMGB1 expression confirmed the release of DAMPs (Figure 3h). These observations indicate that FMBI NP-mediated tumor-catalyzed therapy successfully instigates ICD.

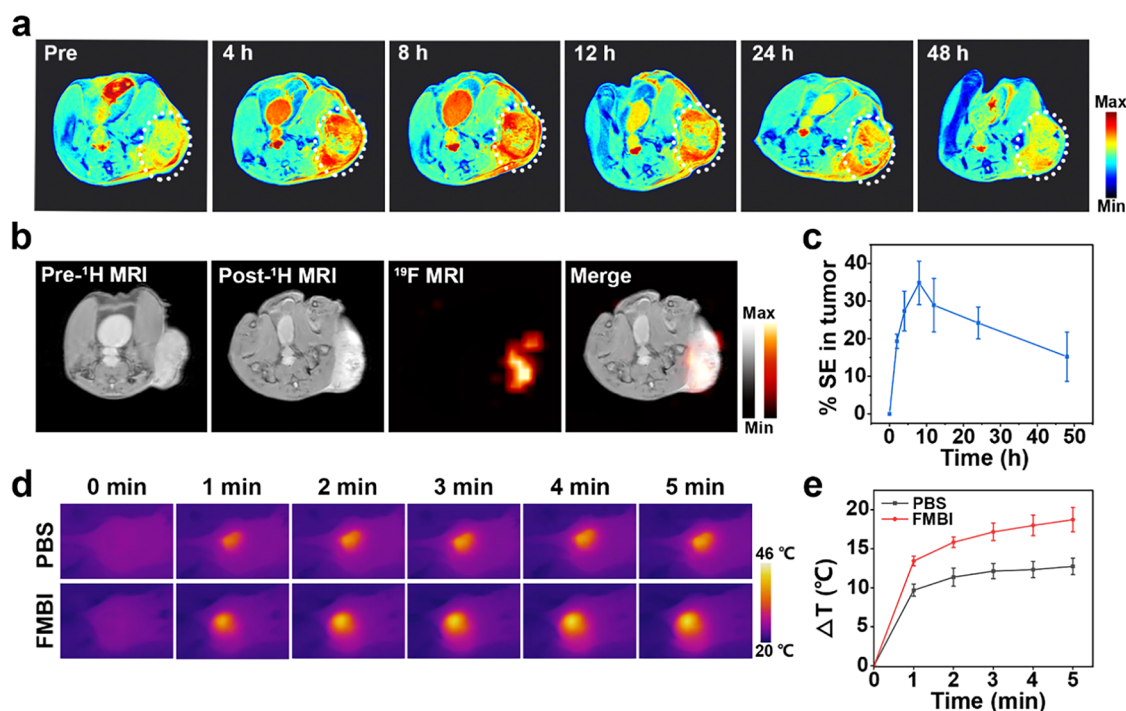


Figure 4. *In vivo* $^1\text{H}/^{19}\text{F}$ MRI imaging and FMBI NP-induced synergistic cancer therapy. (a) *In vivo* ^1H T_1 -weighted MRI images of B16F10 tumor-bearing mice at different time points after *i.v.* injection of FMBI NPs. (b) ^1H T_1 -weighted/ ^{19}F MRI of B16F10 tumor-bearing mice before and after intratumoral injection of FMBI NPs. (c) Quantitative analysis of the ^1H T_1 -weighted MRI signal enhancement rate of tumors after *i.v.* injection of FMBI NPs. (d) Infrared thermal images and (e) corresponding temperature changes at tumor sites in B16F10 tumor-bearing mice after *i.v.* injection of PBS and FMBI NPs, followed by an 808 nm laser irradiation (0.3 W cm^{-2} , 5 min).

FMBI NPs promote ROS generation and GSH consumption in tumor cells through their nanozyme activities and photosensitizing properties, thereby perturbing redox homeostasis. Concurrent interactions between FMBI NPs and GSH result in the liberation of Mn ions. The excessive ROS, coupled with diminished GSH, induces mitochondrial disruption and nuclear double-stranded DNA breaks. Ultimately, apoptosis and ICD occur, accompanied by the release of DAMPs. Finally, the discharged DAMPs along with the resultant Mn^{2+} potentiated subsequent immune responses.

Recent research suggests that Mn^{2+} plays an important role in immune regulation and acts as a potent stimulator to promote DC maturation and M1 macrophage polarization.³⁸ Given that Mn^{4+} reacts with GSH to produce Mn^{2+} , we evaluated the impact of GSH-depletion-induced immune activation mediated by FMBI NPs. Initially, uncommitted RAW264.7 mouse monocyte macrophages, representing the M0 phenotype, were differentiated into the M2 phenotype upon IL-4 stimulation. The induced RAW264.7 macrophages were exposed to supernatants from B16F10 cells subjected to various treatments. The ratio of M2- and M1-type macrophages was analyzed by flow cytometry. Both macrophage subtypes were identified by triple labeling with F4/80, CD86, and CD206 (F4/80 served as a general marker for macrophages, M1-type macrophages: $\text{F4/80}^+ \text{CD86}^+ \text{CD206}^-$, M2-type macrophages: $\text{F4/80}^+ \text{CD86}^- \text{CD206}^+$). The relative abundance of M1 macrophages increased in groups treated with FMBI NPs alone and in combination with a laser, registering an increase from 43.3 to 93.5 and 95.9%, respectively, when compared to the control group (Figure 3i). Flow cytometric analysis demonstrated that FMBI NPs significantly enhanced DC maturation *in vitro* (Figure S17).

The PBS control group exhibited 5.7% mature DCs, while the FMBI NP group showed a maturation rate of 14.5%. When combined with an 808 nm laser irradiation, the DC maturation rate further increased to 27.3%, approximately 1.9-fold higher than that of the FMBI NP group alone. Correspondingly, the release of cytokines such as interferon- γ (IFN- γ) and tumor necrosis factor- α (TNF- α) was also elevated (Figure 3j,k). The enrichment of M1 macrophages, along with increased cytokine levels, suggested that FMBI NPs could promote a phenotypic shift toward M1-type macrophages, thereby triggering an effective immune response. To substantiate that the STING pathway's activation was the cause of these observations, Western blot analyses were performed to assess the expression levels of STING, IRF-3, phosphorylated IRF-3 (p-IRF-3), phosphorylated TBK1 (p-TBK1), and IFN- β in treated B16F10 cells. Notably, the level of expression of these proteins was significantly increased in B16F10 cells treated with FMBI NPs, particularly when combined with laser irradiation (Figure 3b). These findings consistent with flow cytometry and ELISA assay results strongly support that FMBI NPs can effectively activate the STING pathway, thereby facilitating immunomodulation.

2.5. $^1\text{H}/^{19}\text{F}$ MRI/Photothermal Performance of FMBI NPs *In Vivo*. Leveraging the superior *in vitro* ^1H MRI performance, ^1H T_1 -weighted MRI was performed on B16F10 tumor-bearing mice following the intravenous (*i.v.*) injection of FMBI NPs. Interestingly, the tumor region exhibited enhanced contrast in ^1H T_1 -weighted MRI (Figure 4a). At 8 h postinjection, quantitative analysis demonstrated a 34.8% enhancement in the ^1H T_1 -weighted MR signal intensity within the tumor region (Figure 4c). The TME-activated ^{19}F MRI performance *in vivo* was performed following the

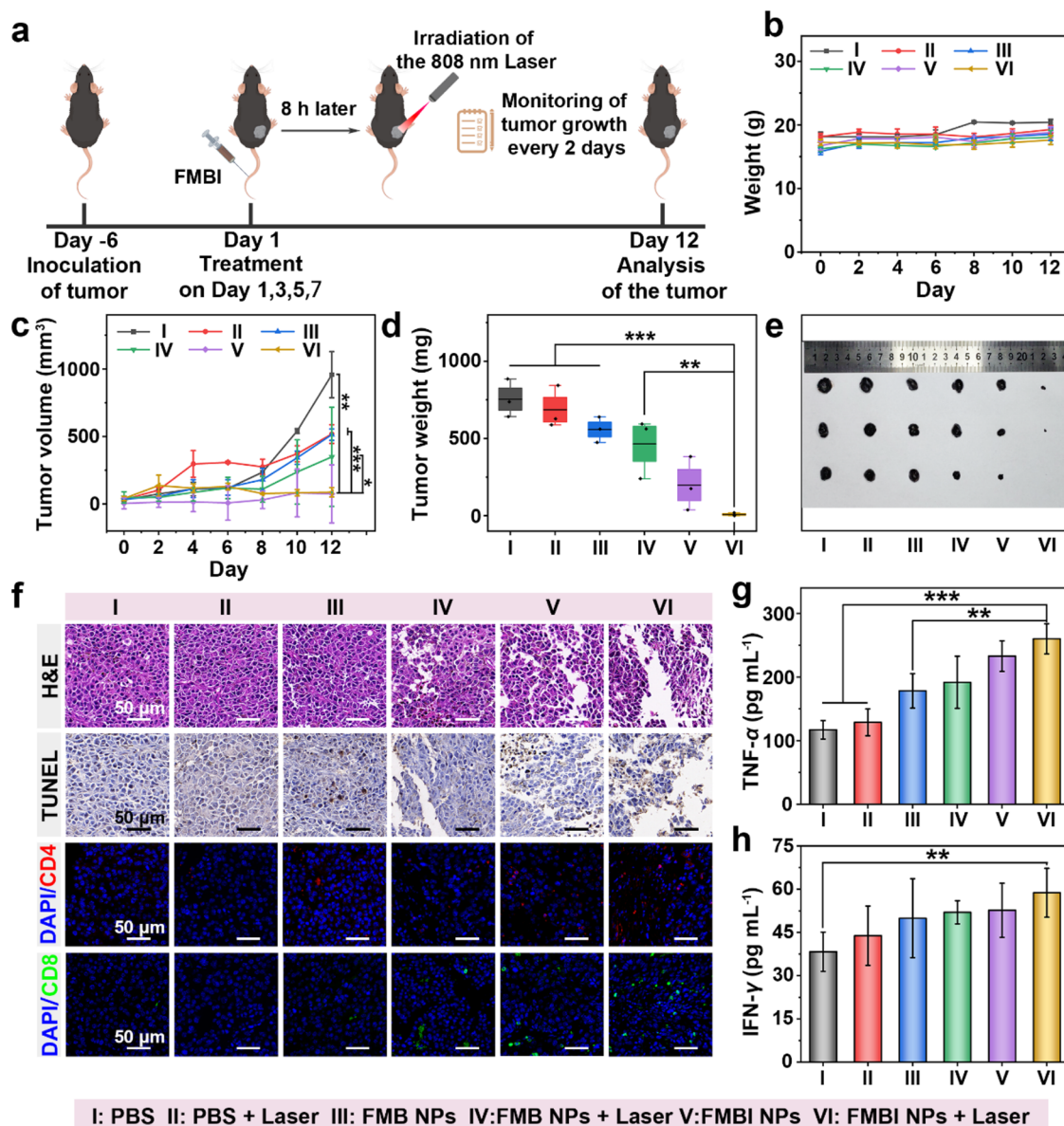


Figure 5. *In vivo* antitumor efficacy and immune activation by FMBI NPs. (a) Schematic depiction of the therapeutic procedure. (b) Body weight, (c) tumor volume, (d) tumor weight changes, and (e) digital photographs of dissected tumors after *i.v.* injection of PBS, FMB, and FMBI NPs with or without laser exposure (0.3 W cm^{-2} , 5 min). (f) H&E, TUNEL, CD4, and CD8 staining images of the tumor sections from mice treated with various drug formulations. Quantitative analysis of the cytokines (g) TNF- α and (h) IFN- γ secreted in B16F10 hormonal mice. n.s. not significant, * $p < 0.05$, ** $p < 0.01$, and *** $p < 0.001$.

intratumoral injection of FMBI NPs. As expected, the ^{19}F MRI signal appeared as a “hot spot” image with zero background noise within the tumor area (Figure 4b). The above results demonstrate that FMBI NPs possess superior tumor imaging capabilities *in vivo*. The photothermal imaging was conducted using an infrared thermal camera to record the temperature changes in different groups subjected to laser irradiation. A stepwise increase in irradiation (5 min, 808 nm, 0.3 W cm^{-2}) duration resulted in a significant enhancement of the photothermal signals within the tumor region, confirming a notable temperature increase by FMBI NPs (Figure 4d,e).

2.6. *In Vivo* Tumor Therapy. Driven by the remarkable ability of FMBI NPs to enhance ROS production and induce immune responses, an *in vivo* therapeutic study was performed to assess their potential in suppressing tumor growth. Subcutaneous melanoma models were established by inoculat-

ing B16F10 cells in the right leg of C57BL/6 mice. Once the tumors reached 40–50 mm^3 , the mice were randomly divided into six groups: PBS (control, I), PBS plus laser (II), FMB (III), FMB plus laser (IV), FMBI (V), and FMBI plus laser (VI).

The treatment protocol is outlined in Figure 5a. After 12 days of treatment, no obvious changes in mouse body weight were observed in any group, implying a negligible acute toxicity of FMBI NPs (Figure 5b). In contrast, the tumor growth patterns differed significantly among the experimental groups. The PBS group exhibited a 31.5-fold increase in tumor volume, whereas FMBI NPs plus laser treatment resulted in only a 2.1-fold increase underscoring its pronounced antitumor efficacy. This effect was further corroborated by tumor weight analysis (Figure 5c–e). The combination of FMBI NPs and laser treatment exerted the strongest tumor suppressive effect. To

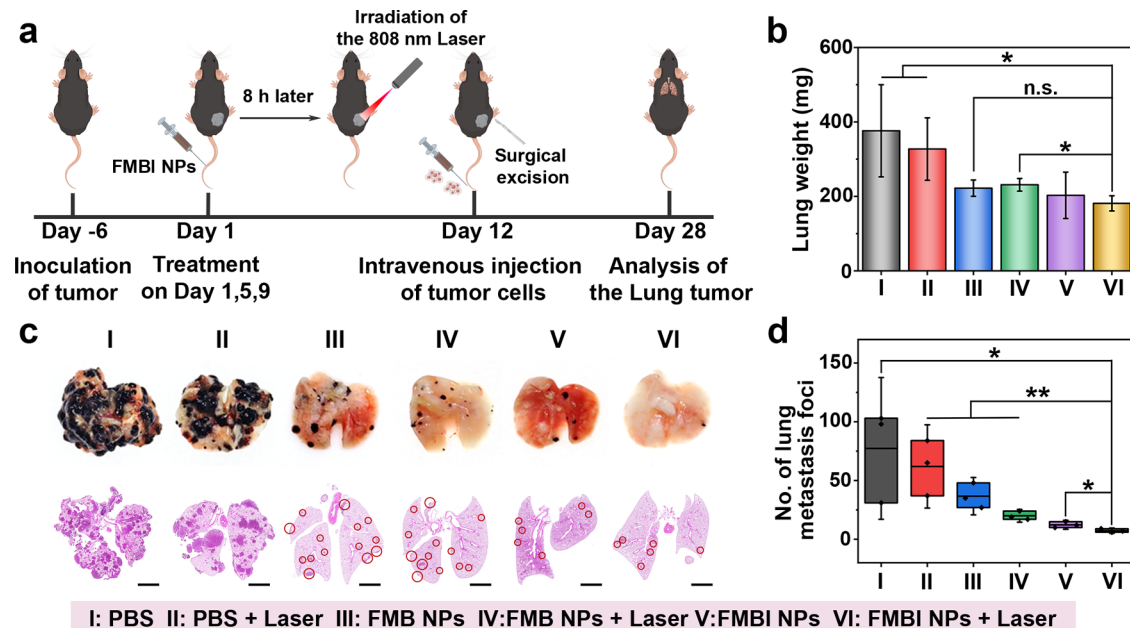


Figure 6. *In vivo* antimetastasis performance by FMBI NPs. (a) Experimental design for lung metastasis inhibition. (b) Lung tissue weight after various treatments. (c) Digital photographs and H&E staining (scale bar: 2000 μm) of excised lungs on day 28 after various treatments. (d) Quantitative analysis of lung nodules. n.s. not significant, * $p < 0.05$, and ** $p < 0.01$.

further assess tumor-killing efficiency, hematoxylin–eosin (H&E) staining and TdT-mediated dUTP nick-end labeling (TUNEL) staining were performed on tumor sections. Additionally, CD4⁺/CD8⁺ T cell infiltration within the tumor microenvironment was also monitored (Figure 5f). The FMBI and FMBI plus laser groups demonstrated a significant increase in the proportion of both CD4⁺ T cells and CD8⁺ T cells. The corresponding cytokines, including IFN- γ and TNF- α , were quantified in the serum of treated mice, revealing elevated levels in both the FMBI and the FMBI plus laser groups (Figure 5g,h). These results further confirmed the immunomodulatory properties of FMBI NPs. Furthermore, hemolysis experiments with FMBI NPs and H&E staining of the mice's major organs demonstrated that the injection of FMBI NPs did not cause any organ damage or hemolysis (Figures S18–S20), confirming excellent biocompatibility at the administered doses.

The impact of FMBI NPs on primary tumor metastasis was evaluated. Subcutaneous melanoma models were established in immunocompetent mice, and 6 days postimplantation, mice were randomized into groups receiving PBS, FMB, or FMBI, with or without laser irradiation. Following treatment, primary tumors were surgically resected, and a lung metastasis model was established via *i.v.* injection of B16F10 cells. On day 28, all mice were sacrificed, and lung tissues were harvested for analysis (Figure 6a). Notably, the lung weight in FMBI NP-treated groups was lower compared to that of other groups (Figure 6b). The lungs of mice in the control group displayed prominent black nodules, indicative of metastasized B16F10 cells in lung tissues. Conversely, the lungs of mice in the FMBI NP-treated groups exhibited markedly fewer nodules. H&E staining results indicated that tumor cell proliferation was significantly inhibited in the FMBI NP-treated groups (Figure 6c,d). TUNEL immunofluorescence staining provided additional evidence, revealing a significant increase in the apoptotic signal of tumor cells following FMBI NP treatment and laser stimulation (Figure S17). Remarkably, the combination of

FMBI NPs and laser treatment almost eliminated lung metastases, underscoring the efficacy of this approach in combating tumor metastasis.

3. CONCLUSIONS

In summary, we have developed a TME-activable manganese-based nanoparticle with multienzyme activities and immunostimulatory capabilities for synergistic therapy and MRI of tumors. The FMBI NPs preferentially accumulate in the tumor, where TME-triggered Mn ion release and concomitant GSH depletion occur. FMBI NPs exhibit multienzyme-like activities, effectively reducing the diffusion barrier and enhancing the local concentration of reactive intermediates. The synergistic effect of chemodynamic therapy promotes the successive generation of ROS, thus killing tumor cells, triggering the ICD of tumor cells, and promoting the maturation of DCs. Mn²⁺ released from the FMBI NPs activates the cGAS-STING signaling pathway, bolsters auto-immune responses, and enhances systemic immune function. Leveraging transition-metal ions as immunostimulants streamlines the creation of diagnostic reagents. *In vivo* studies in B16F10 tumor-bearing mice demonstrated that FMBI NPs could effectively induce antitumor immunity and inhibit lung metastasis. In addition, their tumor-specific accumulation enabled efficient ¹H T₁-weighted and ¹⁹F MRI. The FMBI NPs provide a virtual strategy to concurrently monitor immune activation and improve therapeutic outcomes in melanoma and associated lung metastases.

4. EXPERIMENTAL SECTION

4.1. Synthesis of FMBI NPs. First, the fluorine-accumulated silica nanoparticles (FS NPs) were synthesized according to the reported method. 50 mg of CTAB was dissolved in 6 mL of deionized water and sonicated for 10 min using an ultrasonic cell crusher. 30 μL of PFOB was added to the CTAB aqueous solution and subjected to ultrasonication for 2 h. To remove large aggregates or impurities, the resulting CTAB-PFOB solution was filtered through a 0.45 μm

syringe filter. The filtered solution was added to 23 mL of deionized water and 0.15 mL of NaOH (2 M) solution, stirred, and heated to 70 °C. Next, 0.25 mL of ethyl orthosilicate and 1 mL of ethyl acetate were slowly added to the reaction solution and stirred for 4 h. The obtained materials were centrifuged at 6000 rpm for 5 min, then washed with deionized water at least 3 times. The samples were redispersed in 20 mL of deionized water and stored at 4 °C. The FS NPs were dripped with 1 mg mL⁻¹ of ICG solution and stirred for 16 h in the dark, followed by 3 rounds of centrifugation to obtain FS@ICG NPs. FS@ICG NPs were dispersed in 2-morpholine ethanesulfonic acid (MES) buffer (pH = 6.0, 0.1 M) and vortexed for 3 min. Subsequently, 700 μL of KMnO₄ (5 mM) solution was added dropwise under ultrasonic conditions to react for 30 min, during which the solution color changed from purple to brown. The resulting mixture was centrifuged (5000 rpm, 10 min) to obtain FMB NPs. After wrapping the MnO_x layer, BSA was added in a 1:1 mass ratio, dissolved and sonicated for 10 min, and allowed to stand for an additional 10 min. The final product was washed 3 times with deionized water and dispersed in PBS for storage.

4.2. The CAT-like Activity of FMBI NPs. The CAT-like activity of FMBI NPs was evaluated by measuring the generated oxygen using a dissolved oxygen meter at 37 °C. The CAT-like activity of FMBI NPs was measured by adding different concentrations of FMBI NPs to H₂O₂ solution (pH = 5.4). The generated O₂ solubility (mg L⁻¹) was recorded at different reaction times.

4.3. The POD-like Activity of FMBI NPs. The POD-like activity of FMBI NPs was evaluated using TMB as a probe at 37 °C in the presence of H₂O₂ in PBS solution (0.2 M, pH = 5.4). A UV-vis spectrophotometer was used to record the absorbance of the colorimetric reaction at specific time intervals, which served as an indicator of the POD-like activity.

4.4. The OXD-like Activity of FMBI NPs. The OXD-like activity of FMBI NPs was evaluated using TMB as both the probe and substrate at 37 °C. Briefly, the OXD-like activity of FMBI NPs was measured by adding different concentrations of FMBI NPs and TMB in PBS (final TMB concentration: 1 mM, pH = 5.4). The absorbance at 650 nm was detected by using a UV-vis spectrophotometer.

4.5. FMBI NP-Mediated Consumption of GSH. DTNB solution (2 mM), glutathione (GSH) solution (1, 2, 5, and 10 mM), and deionized water were mixed with FMBI NP solution. The mixtures were maintained at 37 °C with continuous magnetic stirring. The optical absorbance at 412 nm was recorded.

4.6. Cell Culture and Animals. The B16F10, 293T, and RAW264.7 cell lines were purchased from the Cell Bank of the Chinese Academy of Sciences (Shanghai, China). All cells were cultured in a humidified atmosphere containing 5% CO₂ and 95% air at 37 °C. All agents were purchased from Boster Company (China) and filtered with a 0.2 μm sterile filter before use. Female C57BL/6 mice (4–6 weeks old) were obtained from Beiente Biotechnology Co., Ltd. (Wuhan, China).

4.7. Cytotoxicity of FMBI NPs. The cytocompatibility of FMBI NPs in B16F10 and 293T cells was evaluated using the standard CCK-8 assay. The cells were seeded in a 96-well plate (1 × 10⁴ cells per well) and incubated for 24 h. The FMBI NP_s stock solution was diluted to final concentrations of 5, 10, 20, 40, 60, 80, and 100 μg mL⁻¹ using the corresponding cell culture medium and added to the wells. After 24 h, the medium was carefully removed, and the cells were incubated with CCK-8 solution for another 1 h at 37 °C. Finally, absorbance at 450 nm was measured using a microplate reader. Cells cultured in the medium without FMBI NPs served as the control. All data are presented as the mean ± SD, *n* = 3.

4.8. In Vitro ROS Detection. B16F10 cells were treated with PBS, FMBI, and FMBI plus an 808 nm laser for 4 h, followed by multiple washes with PBS. After treatment with 2',7'-dichlorofluorescein diacetate (DCFH-DA, 10 μM), the production of ROS was measured using confocal laser scanning microscopy (CLSM) with a 488 nm excitation (A1R/A1, Nikon, Japan).

4.9. Mitochondrial Membrane Potential. B16F10 cells were cultivated in 20 mm confocal dishes for 24 h, after which the culture medium was replaced with 1 mL of fresh medium. FMBI NPs were

added to the dishes and incubated for 1 and 2 h, respectively, while PBS served as the control. The culture medium was then replaced with 1 mL of fresh medium supplemented with JC-1 probe (10 μg mL⁻¹) and incubated. The mitochondrial membrane potential was assessed by using a confocal microscope with 488 and 561 nm excitations.

4.10. Cell Apoptosis. After B16F10 cells were cultured in 6-well plates for 12 h, the original medium was replaced with 1 mL of fresh medium containing various compounds. Subsequently, specific groups were subjected to an 808 nm laser irradiation, and after a 6 h incubation period, the cells were harvested and stained using an Annexin V/PI kit for 15 min. Finally, apoptosis was analyzed by flow cytometry (CytoFLEX, Beckman).

4.11. Calcein-AM/PI Assay. B16F10 cells were cultivated in 20 mm confocal dishes for 24 h. Then, different substances (PBS, 40 μg mL⁻¹ FMBI NPs, 40 μg mL⁻¹ FMBI NPs plus an 808 nm laser) were added to each well and incubated for 6 h. The cells were washed several times with PBS and stained with Calcein-AM and PI. Finally, the cell apoptosis was detected using CLSM.

4.12. In Vivo ¹H T₁-Weighted/¹⁹F MRI. *In vivo* ¹H T₁-weighted MRI and ¹⁹F MRI were performed using a 9.4 T microimaging system (Bruker Avance 400, Ettlingen, Germany). When the tumor volume reached approximately 80 mm³, the B16F10 tumor-bearing mice were intravenously injected with FMBI NPs (10 mg kg⁻¹) and ¹H T₁-weighted MRI was conducted using a RARE sequence (TR = 500 ms, TE = 10 ms, FOV = 3.5 cm × 3.5 cm, slice thickness = 1 mm, RARE factor = 2, matrix size = 256 × 256) at 0, 2, 4, 8, 12, 24, and 48 h. For ¹⁹F MRI, the tumor was intratumorally injected with 50 μL of FMBI NPs (C_F = 20 mM). ¹⁹F MRI was conducted using a RARE sequence (TR = 1000 ms, TE = 3 ms, FOV = 4.94 cm × 4.94 cm, slice thickness = 14.8 mm, matrix size = 32 × 32, 64 averages).

4.13. In Vivo Therapy. To establish tumor-bearing mice, 4 week old female C57BL/6 mice were subcutaneously injected with 2 × 10⁵ cells into their right leg. Mice bearing B16F10 tumors (approximately 40–50 mm³) were randomly divided into six groups and received the following treatments: I: PBS, II: PBS + Laser, III: FMB NPs, IV: FMB NPs + Laser, V: FMBI NPs, VI: FMBI NPs + Laser, respectively. These mice were intravenously injected with PBS, FMB NPs, and FMBI NPs every 2 days for 6 times at a dose of 10 mg kg⁻¹. Body weight and tumor volume were recorded every 2 days in the morning throughout the treatment period. The tumor volume (*V*) was calculated using the equation $V = (\text{length} \times \text{width}^2)/2$. The major organs and tumors were removed after therapy and preserved in 4% paraformaldehyde for further pathological examination. To assess *in vivo* immunotherapy efficacy, another set of mice with B16F10 tumors (~50 mm³) was randomly allocated into six groups. After the same treatment procedure, the subcutaneous tumors were surgically removed, and the incision was sutured. Additionally, 3 × 10⁵ B16F10 cells were injected into the caudal vein to establish a lung metastasis model. After 16 days, the lungs were dissected and preserved in a 4% paraformaldehyde solution for pathological examination.

■ ASSOCIATED CONTENT

Supporting Information

The Supporting Information is available free of charge at <https://pubs.acs.org/doi/10.1021/acsabm.5c00565>.

Experimental materials and additional experimental results (PDF)

■ AUTHOR INFORMATION

Corresponding Author

Shizhen Chen — State Key Laboratory of Magnetic Resonance Spectroscopy and Imaging, National Center for Magnetic Resonance in Wuhan, Wuhan Institute of Physics and Mathematics, Innovation Academy for Precision Measurement Science and Technology, Chinese Academy of

Sciences, Wuhan 430071, P. R. China; University of Chinese Academy of Sciences, Beijing 100049, P. R. China; School of Biomedical Engineering, Hainan University, Sanya 572019, P. R. China; orcid.org/0000-0002-4883-5790; Email: chenshizhen@wipm.ac.cn

Authors

Qiuyi Xu – State Key Laboratory of Magnetic Resonance Spectroscopy and Imaging, National Center for Magnetic Resonance in Wuhan, Wuhan Institute of Physics and Mathematics, Innovation Academy for Precision Measurement Science and Technology, Chinese Academy of Sciences, Wuhan 430071, P. R. China; University of Chinese Academy of Sciences, Beijing 100049, P. R. China

Sha Li – State Key Laboratory of Magnetic Resonance Spectroscopy and Imaging, National Center for Magnetic Resonance in Wuhan, Wuhan Institute of Physics and Mathematics, Innovation Academy for Precision Measurement Science and Technology, Chinese Academy of Sciences, Wuhan 430071, P. R. China; University of Chinese Academy of Sciences, Beijing 100049, P. R. China

Maosong Qiu – State Key Laboratory of Magnetic Resonance Spectroscopy and Imaging, National Center for Magnetic Resonance in Wuhan, Wuhan Institute of Physics and Mathematics, Innovation Academy for Precision Measurement Science and Technology, Chinese Academy of Sciences, Wuhan 430071, P. R. China; University of Chinese Academy of Sciences, Beijing 100049, P. R. China

Xiaoxun Liu – State Key Laboratory of Magnetic Resonance Spectroscopy and Imaging, National Center for Magnetic Resonance in Wuhan, Wuhan Institute of Physics and Mathematics, Innovation Academy for Precision Measurement Science and Technology, Chinese Academy of Sciences, Wuhan 430071, P. R. China; University of Chinese Academy of Sciences, Beijing 100049, P. R. China

Meiju Sui – State Key Laboratory of Magnetic Resonance Spectroscopy and Imaging, National Center for Magnetic Resonance in Wuhan, Wuhan Institute of Physics and Mathematics, Innovation Academy for Precision Measurement Science and Technology, Chinese Academy of Sciences, Wuhan 430071, P. R. China; University of Chinese Academy of Sciences, Beijing 100049, P. R. China

Lei Zhang – State Key Laboratory of Magnetic Resonance Spectroscopy and Imaging, National Center for Magnetic Resonance in Wuhan, Wuhan Institute of Physics and Mathematics, Innovation Academy for Precision Measurement Science and Technology, Chinese Academy of Sciences, Wuhan 430071, P. R. China; University of Chinese Academy of Sciences, Beijing 100049, P. R. China

Xin Zhou – State Key Laboratory of Magnetic Resonance Spectroscopy and Imaging, National Center for Magnetic Resonance in Wuhan, Wuhan Institute of Physics and Mathematics, Innovation Academy for Precision Measurement Science and Technology, Chinese Academy of Sciences, Wuhan 430071, P. R. China; University of Chinese Academy of Sciences, Beijing 100049, P. R. China; School of Biomedical Engineering, Hainan University, Sanya 572019, P. R. China; orcid.org/0000-0002-5580-7907

Complete contact information is available at:
<https://pubs.acs.org/10.1021/acsabm.5c00565>

Author Contributions

^{||}Q.X. and S.L. contributed equally to this work.

Notes

The authors declare no competing financial interest.

ACKNOWLEDGMENTS

This work was supported by the National Natural Science Foundation of China (U21A20392, 82127802, and 22404064) and the CAS Youth Interdisciplinary Team (JCTD-2022-13). X.Z. acknowledges the support from the Tencent Foundation through the XPLOER PRIZE, and S.C. acknowledges the support from the Young Top-notch Talent Cultivation Program of Hubei Province.

REFERENCES

- (1) Wang, C.; Fan, W.; Zhang, Z.; Wen, Y.; Xiong, L.; Chen, X. Advanced Nanotechnology Leading the Way to Multimodal Imaging-Guided Precision Surgical Therapy. *Adv. Mater.* **2019**, *31*, No. 1904329.
- (2) Bigaj-Józefowska, M. J.; Coy, E.; Załęski, K.; Zalewski, T.; Grabowska, M.; Jaskot, K.; Perrigue, P.; Mrówczyński, R.; Grześkowiak, B. F. Biomimetic Theranostic Nanoparticles for Effective Anticancer Therapy and MRI Imaging. *J. Photochem. Photobiol., B* **2023**, *249*, No. 112813.
- (3) Zhou, Q.; Rao, Q.; Li, H.; Zhang, M.; Zhao, X.; Shi, L.; Ye, C.; Zhou, X. Evaluation of Injuries Caused by Coronavirus Disease 2019 Using Multi-Nuclei Magnetic Resonance Imaging. *Magn. Reson. Lett.* **2021**, *1*, 2–10.
- (4) Beach, M. A.; Nayanathara, U.; Gao, Y.; Zhang, C.; Xiong, Y.; Wang, Y.; Such, G. K. Polymeric Nanoparticles for Drug Delivery. *Chem. Rev.* **2024**, *124*, 5505–5616.
- (5) Tarannum, M.; Vivero-Escoto, J. L. Nanoparticle-Based Therapeutic Strategies Targeting Major Clinical Challenges in Pancreatic Cancer Treatment. *Adv. Drug Delivery Rev.* **2022**, *187*, No. 114357.
- (6) Qu, X.; Zhou, D.; Lu, J.; Qin, D.; Zhou, J.; Liu, H.-J. Cancer Nanomedicine in Preoperative Therapeutics: Nanotechnology-Enabled Neoadjuvant Chemotherapy, Radiotherapy, Immunotherapy, and Phototherapy. *Bioact. Mater.* **2023**, *24*, 136–152.
- (7) Liu, Y.; Wang, L.; Zhang, T.; Wang, C.; Fan, Y.; Wang, C.; Song, N.; Zhou, P.; Yan, C.-H.; Tang, Y. Tumor Microenvironment-Regulating Two-Photon Probe Based on Bimetallic Post-Coordinated MOF Facilitating the Dual-Modal and Deep Imaging-Guided Synergistic Therapies. *ACS Appl. Mater. Interfaces* **2024**, *16*, 12289–12301.
- (8) Xu, H.; Kim, D.; Zhao, Y. Y.; Kim, C.; Song, G.; Hu, Q.; Kang, H.; Yoon, J. Remote Control of Energy Transformation-Based Cancer Imaging and Therapy. *Adv. Mater.* **2024**, *36*, No. 2402806.
- (9) Wang, W.; Chen, C.; Ying, Y.; Lv, S.; Wang, Y.; Zhang, X.; Cai, Z.; Gu, W.; Li, Z.; Jiang, G.; Gao, F. Smart PdH@MnO₂ Yolk-Shell Nanostructures for Spatiotemporally Synchronous Targeted Hydrogen Delivery and Oxygen-Elevated Phototherapy of Melanoma. *ACS Nano* **2022**, *16*, 5597–5617.
- (10) Chen, Q.; Zheng, Y.; Chen, X.; Xing, Y.; Zhang, J.; Yan, X.; Zhang, Q.; Wu, D.; Chen, Z. Bacteria Synergized with PD-1 Blockade Enhance Positive Feedback Loop of Cancer Cells-M1Macrophages-T Cells in Glioma. *Adv. Sci.* **2024**, No. 2308124.
- (11) Zhao, H.; Xu, J.; Feng, C.; Ren, J.; Bao, L.; Zhao, Y.; Tao, W.; Zhao, Y.; Yang, X. Tailoring Aggregation Extent of Photosensitizers to Boost Phototherapy Potency for Eliciting Systemic Antitumor Immunity. *Adv. Mater.* **2022**, *34*, No. 2106390.
- (12) Fu, L.; Ma, X.; Liu, Y.; Xu, Z.; Sun, Z. Applying Nanotechnology to Boost Cancer Immunotherapy by Promoting Immunogenic Cell Death. *Chin. Chem. Lett.* **2022**, *33*, 1718–1728.
- (13) Wang, K.; Li, Y.; Wang, X.; Zhang, Z.; Cao, L.; Fan, X.; Wan, B.; Liu, F.; Zhang, X.; He, Z.; et al. Gas Therapy Potentiates Aggregation-Induced Emission Luminogen-Based Photoimmunotherapy of Poorly Immunogenic Tumors through cGAS-STING Pathway Activation. *Nat. Commun.* **2023**, *14*, No. 2950.

- (14) Khosravi, G. R.; Mostafavi, S.; Bastan, S.; Ebrahimi, N.; Gharibvand, R. S.; Eskandari, N. Immunologic Tumor Microenvironment Modulators for Turning Cold Tumors Hot. *Cancer Commun.* **2024**, *44*, 521–553.
- (15) Suliman, I. H.; Kim, K.; Chen, W.; Kim, Y.; Moon, J. H.; Son, S.; Nam, J. Metal-Based Nanoparticles for Cancer Metalloimmunotherapy. *Pharmaceutics* **2023**, *15*, No. 2003.
- (16) Zhang, K.; Qi, C.; Cai, K. Manganese-Based Tumor Immunotherapy. *Adv. Mater.* **2023**, *35*, No. 2205409.
- (17) Fan, H.; Guo, Z. Tumor microenvironment-responsive manganese-based nanomaterials for cancer treatment. *Coord. Chem. Rev.* **2023**, *480*, No. 215027.
- (18) Huang, A.; Zhou, W. Mn-based cGAS-STING activation for tumor therapy. *Chin. J. Cancer Res.* **2023**, *35*, 19–43.
- (19) Liu, J.; Zhang, Y.; Yang, B.; Jia, Y.; Liu, R. T.; Ding, L.; Shen, Z.; Chen, X. Synergistic Glutathione Depletion and STING Activation to Potentiate Dendritic Cell Maturation and Cancer Vaccine Efficacy. *Angew. Chem., Int. Ed.* **2024**, *63*, No. e202318530.
- (20) Li, Q.; Yang, M.; Sun, X.; Wang, Q.; Yu, B.; Gong, A.; Zhang, M.; Du, F. NIR responsive nanoenzymes via photothermal ablation and hypoxia reversal to potentiate the STING-dependent innate antitumor immunity. *Mater. Today Bio* **2023**, *19*, No. 100566.
- (21) Huang, S.; Gao, Y.; Li, H.; Wang, R.; Zhang, X.; Wang, X.; Huang, D.; Zhang, L.; Santos, H. A.; Yin, Z.; et al. Manganese@Albumin Nanocomplex and Its Assembled Nanowire Activate TLR4-Dependent Signaling Cascades of Macrophages. *Adv. Mater.* **2023**, *36*, No. 2310979.
- (22) Hao, Y.; Zheng, C.; Wang, L.; Zhang, J.; Niu, X.; Song, Q.; Feng, Q.; Zhao, H.; Li, L.; Zhang, H.; et al. Tumor Acidity-Activatable Manganese Phosphate NanoplatforM for Amplification of Photodynamic Cancer Therapy and Magnetic Resonance Imaging. *Acta Biomater.* **2017**, *62*, 293–305.
- (23) Deng, Z.; Xi, M.; Zhang, C.; Wu, X.; Li, Q.; Wang, C.; Fang, H.; Sun, G.; Zhang, Y.; Yang, G.; Liu, Z. Biomaterialized MnO₂ NanoplatforMs Mediated Delivery of Immune Checkpoint Inhibitors with STING Pathway Activation to Potentiate Cancer Radio-Immunotherapy. *ACS Nano* **2023**, *17*, 4495–4506.
- (24) Wang, J.; Wang, J.; Ding, P.; Zhou, W.; Li, Y.; Drechsler, M.; Guo, X.; Cohen Stuart, M. A. A Supramolecular Crosslinker To Give Salt-Resistant Polyion Complex Micelles and Improved MRI Contrast Agents. *Angew. Chem., Int. Ed.* **2018**, *57*, 12680–12684.
- (25) Li, S.; Jiang, W.; Yuan, Y.; Sui, M.; Yang, Y.; Huang, L.; Jiang, L.; Liu, M.; Chen, S.; Zhou, X. Delicately Designed Cancer Cell Membrane-Camouflaged Nanoparticles for Targeted ¹⁹F MR/PA/FL Imaging-Guided Photothermal Therapy. *ACS Appl. Mater. Interfaces* **2020**, *12*, 57290–57301.
- (26) Meng, Y.; Huang, J.; Ding, J.; Zhou, H.; Li, Y.; Zhou, W. Mn-phenolic networks as synergistic carrier for STING agonists in tumor immunotherapy. *Mater. Today Bio* **2024**, *26*, No. 101018.
- (27) Zeng, W.; Yu, M.; Chen, T.; Liu, Y.; Yi, Y.; Huang, C.; Tang, J.; Li, H.; Ou, M.; Wang, T.; et al. Polypyrrole Nanoenzymes as Tumor Microenvironment Modulators to Reprogram Macrophage and Potentiate Immunotherapy. *Adv. Sci.* **2022**, *9*, No. 2201703.
- (28) Wang, R.; Qiu, M.; Zhang, L.; Sui, M.; Xiao, L.; Yu, Q.; Ye, C.; Chen, S.; Zhou, X. Augmenting Immunotherapy via Bioinspired MOF-Based ROS Homeostasis Disruptor with Nanozyme-Cascade Reaction. *Adv. Mater.* **2023**, *35*, No. 2306748.
- (29) Qian, X.; Han, X.; Yu, L.; Xu, T.; Chen, Y. Manganese-Based Functional NanoplatforMs: Nanosynthetic Construction, Physicochemical Property, and Theranostic Applicability. *Adv. Funct. Mater.* **2019**, *30*, No. 1907066.
- (30) Fu, Q.; Wei, C.; Wang, M. Transition-Metal-Based Nanozymes: Synthesis, Mechanisms of Therapeutic Action, and Applications in Cancer Treatment. *ACS Nano* **2024**, *18*, 12049–12095.
- (31) He, H.; Du, L.; Xue, H.; An, Y.; Zeng, K.; Huang, H.; He, Y.; Zhang, C.; Wu, J.; Shuai, X. Triple Tumor Microenvironment-Responsive Ferroptosis Pathways Induced by Manganese-Based Imageable Nanoenzymes for Enhanced Breast Cancer Theranostics. *Small Methods* **2023**, *7*, No. 2300230.
- (32) Sisakhtnezhad, S.; Rahimi, M.; Mohammadi, S. Biomedical Applications of MnO₂ Nanomaterials as Nanozyme-Based Theranostics. *Biomed. Pharmacother.* **2023**, *163*, No. 114833.
- (33) Lin, H.; Tang, X.; Li, A.; Gao, J. Activatable ¹⁹F MRI NanoprobEs for Visualization of Biological Targets in Living Subjects. *Adv. Mater.* **2021**, *33*, No. 2005657.
- (34) Nakamura, T.; Matsushita, H.; Sugihara, F.; Yoshioka, Y.; et al. Activatable ¹⁹F MRI Nanoparticle Probes for the Detection of Reducing Environments. *Angew. Chem., Int. Ed.* **2015**, *54*, 1007–1010.
- (35) Li, D.; Ha, E.; Zhou, Z.; Zhang, J.; Zhu, Y.; Ai, F.; Yan, L.; He, S.; Li, L.; Hu, J. "Spark" PtMnIr Nanozymes for Electrodynamically Boosted Multienzymatic Tumor Immunotherapy. *Adv. Mater.* **2023**, *36*, No. 2308747.
- (36) Zhang, C.; Wang, X.; Du, J.; Gu, Z.; Zhao, Y. Reactive Oxygen Species-Regulating Strategies Based on Nanomaterials for Disease Treatment. *Adv. Sci.* **2020**, *8*, No. 2002797.
- (37) Zhang, Y.; Ma, Q.; Yan, Y.; Guo, C.; Xu, S.; Wang, L. Intratumoral Glutathione Activatable NanoprobEs for Fluorescence and ¹⁹F Magnetic Resonance Turn-On Imaging. *Anal. Chem.* **2020**, *92*, 15679–15684.
- (38) Chen, C.; Tong, Y.; Zheng, Y.; Shi, Y.; Chen, Z.; Li, J.; Liu, X.; Zhang, D.; Yang, H. Cytosolic Delivery of Thiolated Mn-cGAMP Nanovaccine to Enhance the Antitumor Immune Responses. *Small* **2021**, *17*, No. 2006970.